Iterative Methods for Waveform Control in Magnetic Measurement Systems

Patrick Fagan, Benjamin Ducharne, Stanislaw Zurek, Mathieu Domenjoud, Anastassios Skarlatos, Laurent Daniel, Christophe Reboud

Iterative methods for waveform control in magnetic measurement systems

Patrick Fagan, Benjamin Ducharne, Stanislaw Zurek, Mathieu Domenjoud, Anastasios Skarlatos, Laurent Daniel, Christophe Reboud

***Abstract*—Magnetic losses in a ferromagnetic lamination can be separated into three contributions. Bertotti theoretically assessed this distribution at the end of the 20th century in the Statistical Theory of Losses (STL), triggering significant progress in understanding the dissipation mechanisms. Recent studies have shown the possibility of reconstructing a hysteresis cycle from the high-frequency Barkhausen noise signal. Applying STL to the Barkhausen noise cycles has never been done before. Still, it could help establish a parallel with the measurement of the magnetization cycle versus frequency and the energy loss. However, STL analysis in its ultimate description requires sinusoidal flux density, while Barkhausen noise measurements are usually done with a constant excitation slope. Multiple magnetic flux density control methods were described in the literature and are reviewed in this manuscript. However, the Barkhausen noise context, requiring high-frequency sampling during the magnetization cycle, is more constraining. Therefore, specific performance criteria were considered, followed by numerical tests to determine the most adapted method to a Barkhausen STL description. Eventually, the Proportional Iterative Learning Control (P-ILC) gave the highest satisfaction rate and was chosen for experimental tests. Some of these experimental results are provided in the manuscript discussion together with suggestions for convergence speed improvement. It is, for instance, recommended to increase the gain near saturation, where the system response is poor.**

***Index Terms*—Magnetic Barkhausen noise energy, waveform control, feedback, magnetic losses**

I. Introduction

Magnetic cores are omnipresent in electrical energy conversion and transport. Losses inevitably happen while magnetic cores operate and are a significant cause of inefficiency. During one magnetization cycle, these losses are equivalent to the area of the $B_a(H_{surf})$ hysteresis cycle obtained by plotting the flux density B_a averaged through the tested specimen cross-section as a function of the tangent surface excitation field H_{surf} [1]:

$$P = \oint B_a(H_{surf}) \cdot dH_{surf} \quad (1)$$

The first attempts for the hysteresis losses prediction trace back to Steinmetz's model (Eq. 2) [2][3]. This empirical relation was limited to sinusoidal B_a conditions and stated that iron losses followed a fractional power "law" of both frequency f and $B_{a_{max}}$ (peak value of sinusoidal B_a):

$$P = k \cdot f^a \cdot B_{a_{max}}^b \quad (2)$$

where k, a, and b were three constant parameters depending on the nature and geometry of the magnetic circuit. Loss separation was initially proposed in 1924 with Jordan's work [4], who assumed that magnetic core losses could be divided (Eq. 3) in a static contribution P_{st} and a dynamic contribution related to classical eddy current loss P_{cl} [4]-[6]:

$$P = P_{st} + P_{cl} = \alpha \cdot f + \beta \cdot f^2 \quad (3)$$

where α and β were fit parameters. This simple approach was later improved by adding an excess loss term to match the experimental data, wrongly approximated by Eq. 3 (grain-oriented electrical steels FeSi GO, etc. [7]). Initially, the physical justification for the additional contribution was unknown, and it was even referred to as "anomalous" loss. It was obtained by either modifying β or simply adding a third contribution or "excess" loss (P_{exc}) [8]:

$$P = P_{st} + P_{cl} + P_{ex} \quad (4)$$

This empirical method found theoretical foundations from Bertotti Statistical Theory of Losses (STL) [9], expressed in terms of power in Eq. 5 or energy in Eq. 6 (a_{st}, a_{cl} and a_{exc} are fitting parameters):

$$P = a_{st} \cdot f + a_{cl} \cdot f^2 + a_{exc} \cdot f^{\frac{3}{2}} \quad (5)$$

$$W(f) = \frac{P}{f} = a_{st} + a_{cl} \cdot f + a_{exc} \cdot \sqrt{f} \quad (6)$$

STL is an advanced theoretical method that brought significant progress in understanding the magnetization mechanisms [10]-[16]. It is, however, worth mentioning that STL supposes a full flux penetration which restricts its domain

Patrick Fagan, Anastasios Skarlatos and Christophe Reboud are with LIST, CEA, CNRS, Université Paris-Saclay, CEA Saclay, 91191 Gif-sur-Yvette, France.

Benjamin Ducharne is with ELyTMaX IRL3757, CNRS, Univ Lyon, INSA Lyon, Centrale Lyon, Université Claude Bernard Lyon 1, Tohoku University, Sendai, Japan and with LGEF, Laboratoire de Génie Electrique et Ferroélectricité, INSA Lyon, France. (e-mail: benjamin.ducharne@insa-lyon.fr).

Stanislaw Zurek is with Megger Instruments, Archcliffe Road, Dover, CT17 9EN, United Kingdom.

Mathieu Domenjoud and Laurent Daniel are with Université Paris-Saclay, CentraleSupélec, CNRS, Group of Electrical Engineering-Paris (GeePs), 91192, Gif-sur-Yvette, France and with Sorbonne Université, CNRS, Group of Electrical Engineering-Paris (GeePs), 75252, Paris, France.

of validity to approximately 100 Hz for a typical FeSi GO (thickness = 300 µm).

Recent works [17]-[19] have demonstrated the feasibility of plotting hysteresis cycles from Barkhausen noise measurement. For this, the so-called Magnetic Barkhausen Noise energy MBN_{energy} (Eq. 7) is plotted as a function of H_{surf}.

$$MBN_{energy}(t) = \nu \cdot \int_0^t \text{sign}\left(\frac{dH_{surf}}{ds}\right) \cdot V_{MBN}^2(s) \cdot ds \quad (7)$$

ν is a normalization coefficient and V_{MBN} the magnetic Barkhausen noise voltage drop across the sensor coil. Comparably to the classic $B_a(H_{surf})$, $MBN_{energy}(H_{surf})$ hysteresis cycles depend on the excitation frequency and thus reflect physical properties. It is, therefore, tempting to apply STL to these alternative cycles and get additional insights regarding the physics of the magnetization mechanisms. MBN_{energy} is linked predominantly to the magnetic domain wall motions; thus, in the MBN_{energy} STL, the classical loss contribution, related to the macroscopic eddy currents and first-order-frequency-dependent, should be negligible. Hence, the frequency dependency of the MBN_{energy} hysteresis cycle energy is expected to be written as in Eq. 8:

$$W_{MBN_{energy}}(f) = b_{st} + b_{exc} \cdot \sqrt{f} \quad (8)$$

with b_{st} and $b_{exc,}$ two constants. Eq. 8 is purely hypothetical and has never been validated by comparison to experimental results. By increasing the magnetization frequency, the available frequency band of the MBN spectral density is expected to shift upward. Still, this effect remains unclear and the comparison with STL is expected to bring clarification. Even if STL was originally developed, for the sake of simplicity, by assuming that the magnetization process occurs under controlled macroscopic constant induction derivative (triangular induction), the ensuing formulation was successively modified to comply with sinusoidal and generic induction waveform. Eq. 6 supposes this condition to be respected [15]. In the case of Barkhausen noise measurements, either the excitation current or the magnetic excitation H_{surf} is usually imposed triangular [21][22] and measurements rarely done under sinusoidal flux density. $B_a(H_{surf})$ and $MBN_{energy}(H_{surf})$ can be obtained from the same experimental setup. Therefore, a suitable method for the flux density control during Barkhausen noise measurement can be inspired by published work related to standard hysteresis characterizations [23]-[30]. Still, additional constraints owed to Barkhausen noise measurement have to be considered before setting the most adapted method. A magnetic characterization setup contains two non-linear elements (the inductor yoke used to drive the magnetic field H_{surf} and the tested sample). Analytical solutions are sometimes proposed for setting the induction control system. Still, the effect of hysteresis and the to-be-measured properties of the specimen makes them approximative hence iterative methods prevail. The focus of this paper is to examine a wide range of digital feedback methods found in the literature to assure a sinusoidal flux density during hysteresis measurements and select the most appropriate one for the specific context of the Barkhausen noise STL application. Comparisons exist in the literature [31], but they are limited to two or three methods and never deal with the specific Barkhausen noise perspective. The study is restricted to digital feedback methods [24]-[30]. Even if widespread before the proliferation of computers, the analog feedback methods [30][32][33] are poorly tunable and less robust since they rely on discrete components whose values can be challenging to set, especially if heated. Analog systems work in real-time. Perturbations cannot be anticipated, and high precisions cannot be reached on a wide range of frequencies and materials. Other problems can arise if the system is strongly non-linear and has unstable feedback [20]. It should also be noted that high-gain high-bandwidth analog (real-time) feedback can suppress large-amplitude Barkhausen noise activity [1][20]. For the same reasons, this paper will not consider hybrid methods (obtained by combining digital and analog feedback methods [34][35]).

II. Review of Iterative Feedback Methods

A. Performance criteria

This study aims to define and test the most efficient magnetic flux density control method in the context of the MBN_{energy} hysteresis cycle characterization and STL application [21][22][36]. To obtain adapted comparisons and reach our objective, a specific series of criteria has been defined:

- Number of iterations: a reduced number of iterations is important, especially in the low-frequency range where a measure can take several minutes and generate large data files complex to process. It is also critical in the high-frequency range, where thermal transfers due to the magnetic losses can affect the experimental conditions and the magnetic response of the material.
- Accuracy: Convergence should be reached with a minimum error. Error estimations can take different forms, including relative Euclidean difference, form factor difference, Pearson dissimilarity, total harmonic distortion, etc.
- Number of parameters: Feedback control parameters must be tuned for each new experimental situation. Optimizing a large number of parameters requires a lot of experimental data.
- Robustness: the feedback method should remain undisturbed by external stimuli, including white noises, drifts, and offsets.
- Memory allocation and computation time efficiency: The ideal feedback method computes an iteration with reduced time and limited memory capacity. This criterion is especially detrimental for techniques based on square matrix inversion requiring high computation capacity and large memory allocation.
- Universality: This criterion is related to the capability of providing satisfactory results in different experimental conditions without extensive calibrations processes.

A feedback method providing a positive answer to all the criteria listed above does not exist. Many approaches have been described in the literature [21]-[27], and each technique can perform well in specific conditions. This study aims to compare these methods to find the most suitable feedback technique in the particular context of the $MBN_{energy}(H_{surf})$ hysteresis cycles characterization.

B. Detailed description of iterative feedback methods

Let us introduce the feedback notation and a general feedback scheme (Fig. 1)

- $Y_G(t)$ is the reference, i.e. the ideal desired goal output (at time t).

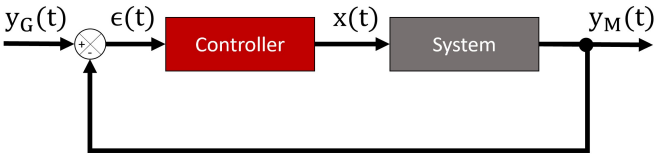

Fig. 1 – Feedback structure.

- $y_M(t,j)$ is the measured output of iteration j (at time t).
- $\epsilon(t,j)= y_G(t) - y_M(t,j)$ is the error of j-th iteration (at time t).
- $x(t,j)$ is the system input of j-th iteration (at time t).

1) **Iterative Learning Control (ILC)**

A straightforward iterative method for the control of a non-linear system can be derived from the classical real-time Proportional Integral Derivative (PID) technique:

$$x(t) = K_P \cdot \epsilon(t) + K_I \cdot \int_0^t \epsilon(s)\, ds + K_D \cdot \frac{d\epsilon}{dt} \quad (9)$$

with K_p, K_I, and K_D, the proportional, integral, and derivative gains. The iterative PID method has been described by several authors, including Gruebler et al. in [37], and consists in:

$$x(t, j+1) = x(t, j) + \Delta x(t, j) \quad (10)$$

$$\Delta x(t, j) = K_P \cdot \epsilon(t, j) + K_I \cdot \int_0^t \epsilon(s, j)\, ds + K_D \cdot \frac{d\epsilon}{dt}(t, j) \quad (11)$$

In their simplest form (proportional correction only), the above equations can be simplified, which leads to the Proportional-Iterative Learning Control formulation P-ILC [37]:

$$x(t, j+1) = x(t, j) + K_P \cdot \epsilon(t, j) \quad (12)$$

The phase-lead ILC method is similar to P-ILC but involves the addition of a constant delay τ in the error term [38][39]:

$$x(t, j+1) = x(t, j) + K_P \cdot \epsilon(t + \tau, j) \quad (13)$$

P-ILC is simple; the inputs are reduced to $\epsilon(t,j)$, and parameters to K_p. Its implementation is very straightforward, and, like classic PID, it can be very robust with the right choice of K_p. However, the choice between high gain/fast convergence and small gain/no divergence makes the optimization tricky, typically ending with a slower convergence speed at the benefit of better robustness.

2) **Fourier Series Proportional-Iterative Learning Control (FSP-ILC)**

Switching from the time domain to the frequency domain can be highly beneficial by simplifying mathematical operations. The Fourier transform being linear, Eq. 14 becomes 15:

$$x(t, j+1) = x(t, j) + K_P \cdot [y_G(t) - y_M(t, j)] \quad (14)$$

$$X(f, j+1) = X(f, j) + K_P \cdot [Y_G(f) - Y_M(f, j)] \quad (15)$$

Where $X(f,j)$ is the Fourier transform of $x(t,j)$. Fourier transforms lead to complex numbers, and FSP-ILC works with complex number formalism. While Fourier Distribution Iterative Learning Control FDP-ILC would apply Eq. 15 to the whole frequency spectrum, FSP-ILC is limited only to the excitation frequency's multiples (f_{exc}) and can even be reduced to those of substantial contribution. Eq. 16 gives FSP-ILC's equation when $k \in [1 – M]$:

$$X(k \cdot f_{exc}, j+1) = X(k \cdot f_{exc}, j) + K_P \cdot [Y_G(k \cdot f_{exc}) - Y_M(k \cdot f_{exc}, j)] \quad (16)$$

FSP-ILC performance is relatively close to those of P-ILC. The main advantage of the former is its ability to ignore all the high-frequency components (> $M \cdot f_{exc}$), including white noise and power source oscillations, especially when f_{exc} is low. Its main drawback is the two Fourier transforms and the sum of complex numbers required per iteration, slowing down the control speed and inducing limitations in the low-frequency range. The computation time can be reduced significantly if Fast Fourier Transform (FFT) is employed, but at the additional restriction that the number of samples in the waveform becomes a power of 2.

3) **Phase Correction by determination of Measure-Goal Delay (PhC-MGD)**

P-ILC performances depend on the power supply dynamic response and capability to generate x without undesired phase lag. A phase correction is sometimes needed to increase the feedback performance. For this, several methods have been proposed, including PhC-MGD, a technique described by Stupakov et al. in [21]. In this method, a preliminary step increases x until y_M reaches the required amplitude. This operation is achieved by a P-ILC correction of gain modulated by y_M's amplitude identified at the previous stage (Eq. 17):

$$x(t, j+1) = x(t, j) \cdot \left\{1 + \frac{K_P \cdot [\max(y_G) - \max(y_M(j))]}{\max(x(j))}\right\} \quad (17)$$

Once y_M reaches the required threshold, x is recalculated through a sum of two weighted contributions (G_{ph} is the weight), the corrected phase contribution x_{ph} and the corrected amplitude contribution x_{ampl}:

$$x(t, j+1) = G_{ph} \cdot x_{ph}(t, j+1) + (1 - G_{ph}) \cdot x_{ampl}(t, j+1) \quad (18)$$

where x_{ph} is calculated as follows:

- the measure is normalized according to the targeted waveform:

$$y_M = y_M \cdot \frac{\max(y_G)}{\max(y_M)} \quad (19)$$

- the resulting signal is divided into sections where the targeted waveform is monotonic,
- the delay ø(t) (see Fig. 2) between the targeted waveform and the measurement is estimated.
- ø(t) is applied simultaneously to y_M and x and leads to the delayed versions y_{req} and x_{ph}:

$$\begin{cases} x_{ph}(t, j+1) = x(t + ø(t), j) \\ y_{req}(t, j+1) = y_M(t + ø(t), j) \end{cases} \quad (20)$$

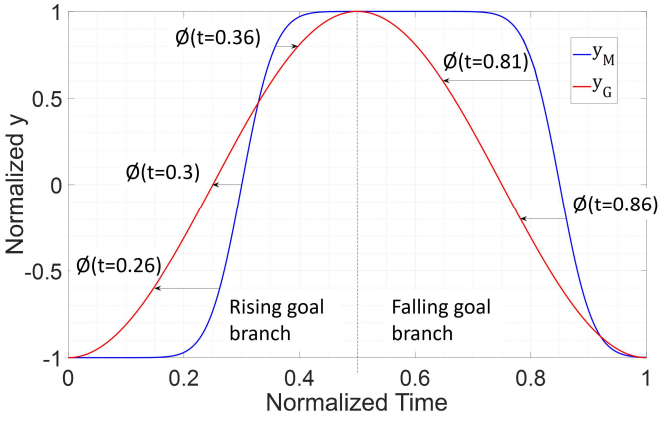

Fig. 2 – PhC-MGD delay illustration.

X_{ampl} is obtained from a P-ILC method of y_{req} targeted waveform instead of the usual y_G:

$$x_{ampl}(t, j+1) = x(t, j) + K_P \cdot [y_{req}(t, j) - y_M(t, j)] \quad (21)$$

In [21], G_{ph} has a non-zero value exclusively in the high-frequency range when phase shift exists. The main drawback of PhC-MGD is the normalization step, which flattens the measurement signal in the presence of undesired noise peaks and makes the phase delay estimation complicated. This noise issue has been solved partially in [21] by taking one thousand points per cycle, interpolating H_{surf} with a cubic spline, and smoothing B_a with a numerical filter.

4) **Phase Correction by P-ILC on angles (PhC-P-ILC)**

In 2005, Zurek et al. in [40] proposed a correction method described as the combination of two steps:

- An amplitude correction leading to x_* (an intermediary variable) and assimilated to a P-ILC of effective gain inversely proportional to y_M's amplitude:

$$x_*(t, j+1) = x(t, j) + K_P \frac{\epsilon(t,j)}{\max(y_M(j))} \quad (22)$$

$$x_*(t, j+1) = x(t, j) + \frac{K_P}{\max(y_M(j))}[y_G(t) - y_M(t, j)] \quad (23)$$

- A phase correction applied through a phase delay function F:

$$x(t, j+1) = F[x_*(t, j+1)] \quad (24)$$

During this phase correction, every involved quantity is expressed by its Fourier series (Eq. 25 to 28):

$$y_M(t, j) = a_0 + \sum_{k=1}^{M} a_k(j) \sin[2\pi k f_1 t + \phi_k(j)] \quad (25)$$

$$y_G(t) = b_0 + \sum_{k=1}^{M} b_k \sin[2\pi k f_1 t + \psi_k] \quad (26)$$

$$x_*(t, j) = c_0 + \sum_{k=1}^{M} c_k(j) \sin[2\pi k f_1 t + \theta_k(j)] \quad (27)$$

$$I(t, j) = d_0 + \sum_{k=1}^{M} d_k(j) \sin[2\pi k f_1 t + \beta_k(j)] \quad (28)$$

where M is the number of considered harmonics, f_1 is the targeted waveform frequency, a_i, b_i, c_i, and d_i are the Fourier amplitudes, and I the output current. I and x are linked through Eq. 29. They are identical if the source is an ideal unity gain amplifier ($G_{source} = 1$):

$$I(t, j) = G_{source}(s) \cdot x(t, j) \quad (29)$$

$ø_i$, ψ_i, θ_i and β_i, are the Fourier phase lags associated to a_i, b_i, c_i, and d_i. With this formalism:

$$x(t, j+1) = F[x_*(t, j+1)] = \sum_{k=0}^{M} c_k(j+1) \cdot \sin[2\pi k f_1 t + \theta_k(j+1) + \alpha_k(j+1)] \quad (30)$$

and,

$$\alpha_k(j+1) = \alpha_k(j) + K_\alpha \cdot (\psi_k - \beta_k(j)) \quad (31)$$

α_k is the k^{th} harmonic applied phase lag, and K_α a proportional gain. PhC-P-ILC reduces the influence of the power source but works in the Fourier domain, which means time-consuming direct and inverse transformations (especially when the number of considered data points is large). The implementation is complex compared to P-ILC.

5) **Non-linear correction with a Quasi-Newtonian Method (QNM)**

In 2008, Yamamoto et al. in [41] described QNM, a non-linear iterative control method derived from the BFGS-like technique published by Li and Fukushima [42] a few years before. The BFGS algorithm (Broyden-Fletcher-Goldfarb-Shanno) can be described as a line search optimization method, and Li's method is the derivative-free version of this algorithm.

At each iteration, several variables need to be evaluated: an N·N Hessian matrix B_j (where N is the size of vector x), y_M, y_G, and ϵ_M.

$$\epsilon_M(t, j) = f[x(t, j)] \quad (32)$$

B_0 (initialization at j = 0) is defined as an identity matrix, and f a function to minimize. For each iteration j, the following algorithm is run:

- the search direction p_j is found by solving:

$$B_{j-1} \cdot p_j = -\epsilon_{M_{j-1}} \quad (33)$$

- the step-size α_j is set to 1, a new measure is made with:

$$x_{temp} = x_{j-1} + \alpha_j \cdot p_j \quad (34)$$

which leads to obtaining y_{Mtemp} and ϵ_{temp}.

- if the error is not small enough $\left(\left\|\epsilon_{M_{temp}}\right\| > \rho \cdot \left\|\epsilon_{M_{j-1}}\right\| - \sigma_2 \cdot \left\|p_j\right\|^2\right)$ the previous step is repeated, but α_j is contracted by a factor $\beta \in [0 - 1]$:

$$\alpha_j = \beta \cdot \alpha_j \quad (35)$$

This step is repeated until $\left(\left\|\epsilon_{M_{temp}}\right\| > (1 + \eta_j) \cdot \left\|\epsilon_{M_{j-1}}\right\| - \sigma_1 \cdot \left\|\alpha_j \cdot p_j\right\|^2\right)$

- B_j is updated according to Eq. 36 below:

$$B_j = B_{j-1} + \theta_j \cdot \frac{(\epsilon_{temp} - \epsilon_{j-1}) - B_{j-1}.(x_{temp} - x_{j-1})}{\left\|\epsilon_{temp} - \epsilon_{j-1}\right\|^2} \cdot (x_{temp} - x_{j-1})^T \quad (36)$$

where θ_j is set to ensure B_j is not singular.

- x_j, and y_j are set from the temporary variables: $x_j = x_{temp}, y_j = y_{temp}$

QNM differs from [42] by a different initialization of α_j:

$$\alpha_j = \frac{1}{1 + \left\|\epsilon_{j-1}\right\|} \quad (37)$$

QNM converges faster than P-ILC, especially near saturation, where P-ILC requires hundreds of iterations. But, QNM suffers from several weaknesses, including the excessive number of parameters: the fixed parameters ρ, β, $\bar{\theta}$, σ_1, σ_2 and the variable ones such as η and θ modified for every iteration:

$$\sum_{k=0}^{+\infty} \eta_j < \eta < \infty \quad (38)$$

$$\left|\theta_{j-1} - 1\right| < \bar{\theta} \quad (39)$$

Another drawback is the computationally expensive inversion of square matrix. Convergence speed is also impacted by the multiple measurements needed per iteration. Hence, QNM is inadequate in the very-low-frequency range.

6) **Least-Square Method for a $H_{surf}(B_a)$ Polynomial Identification (LSM-PI)**

In 2011, Anderson [43] proposed LSM-PI, an alternative iterative method which can be summarized as follows:

- Like in PhC-MGD, the data set y_M is divided into monotonic sections, and an offset is applied to obtain $x(y_M=0)=0$ for each section.

- $X(y_M)$ is defined for every section and approximated by a high-order polynomial (up to order of 30 in [40]):

$$x(y_M) \approx \sum_{i=1}^{30} a_i \cdot y_M^i(t) \quad (40)$$

- a_i coefficients are determined with a least-squares method, and a phase term is considered for the hysteretic behavior.
- x is calculated from Eq. 40 by replacing y_M by y_G (Eq. 41):

$$x(t) = \sum_{i=1}^{30} a_i \cdot y_G^i(t) \quad (41)$$

This method converges with a minimal number of iterations (just three as claimed in [43]), but its performance relies heavily on the order of the polynomial function. Many oscillation issues are noticed (especially near saturation, where the magnetic permeability μ is low, but the $H_{surf}(B_a)$ slope is high). The least-squares optimization is computationally expensive, especially if many sampling points are considered. This problem can be lessened by expressing $H_{surf}(B_a)$ in a different orthonormal system. Moreover, this method assumes that $H_{surf}(B_a)$ is bijective, which is not the case if the maxima of H_{surf} and B_a are not simultaneous (as it is in the high-frequency range). In that case, a phase delay must be considered to avoid wrong results from the least-square optimization.

7) **Other methods**

It is not possible to provide an exhaustive list of all feedback methods and their modifications described in the scientific and technical literature. The main techniques introduced in the sections above have been numerically implemented and tested in this study. They have been chosen for their singularities and originalities, but more methods exist, and even if not detailed nor tested, they are worth mentioning in this manuscript:

- In 2016, Zhang et al. in [44] described a proportional corrector, working in the frequency domain and in which both magnitudes and phases are corrected. For every harmonic, the correction can be written as:

$$X_{mag} = K_{P_{mag}} \cdot \left[Y_{G_{mag}} - Y_{M_{mag}}\right] + K_{I_{mag}} \cdot \int \left(Y_{G_{mag}} - Y_{G_{mag}}\right) dt \quad (42)$$

$$X_{ph} = K_{P_{ph}} \cdot \left[Y_{G_{ph}} - Y_{M_{ph}}\right] + K_{I_{ph}} \cdot \int (Y_{G_{ph}} - Y_{M_{ph}}) dt \quad (43)$$

Then, x(t,j+1) is written as a Fourier series thanks to the X_{mag} and X_{ph} coefficients. This method shares the same strengths and weaknesses as FSP-ILC but is also very sensitive to the non-linear behavior of the ferromagnetic sample. In [44], this issue is solved by correcting the calculated phases based on a look-up table. Unfortunately, no details are provided about the method for constructing such a look-up table.

- In [45], White et al. use a proportional derivative PD-ILC method to control the excitation current I (assuming that H_{surf} is proportional to I and the resistances and inductances values perfectly known). Good results are obtained, but compared to P-ILC the implementation is complex and requires detailed knowledge of the experimental conditions and their evolution during the test, which is not trivial considering that the inductance varies significantly with the level of excitation.
- In [46], Bosack et al. start from Jiles-Atherton's model and assumes the magnetization M can be written as:

$$\frac{dM}{dt} = g(H_{surf}, M, t) + f(H_{surf}, M, u) \quad (44)$$

where f and g are two known functions, and u is a control variable, defined by:

$$\frac{dH_{surf}}{dt} = \frac{dH_0}{dt} + \frac{dH_c}{dt} = \frac{dH_0}{dt} + u \quad (45)$$

H_0 is the ambient field excitation, and H_c is the corrected contribution. The resolution of the system gives:

$$u = -\frac{dH_0}{dt} - K_P \cdot f(M) \cdot (M - M_{goal}) \quad (46)$$

Eq. 46 looks like a K_p proportional correction. No details about the practical implementation are given in [46], except the use of a real-time PID corrector. The estimations of f and g rely on identification steps, and calibration must be made each time the whole system changes, which can be time-consuming, especially if recalibration is to be applied at each new measurement frequency. Finally, non-linear algorithms have also been described in contexts unrelated to magnetic waveform control (electrohydraulic molding machine in [47] or lithographic apparatus in [48]). Like QNM, these methods require matrices inversion, limiting the experimental sampling rate and leading to feedback control incompatible with MBN_{energy} characterizations.

C. Required precision criterion

All the methods described in this section have been developed to comply with international magnetic characterization standards, and different criteria have been proposed for their validation. It is worth noting that some of these criteria apply to the time derivative z of the targeted waveform x.

These criteria include:

- The relative Euclidean Difference :

$$d_{red}(x, y) = \sqrt{\frac{\int [x(t) - y(t)]^2 dt}{\int x(t)^2 \, dt}} \quad (47)$$

- The Form Factor (applied only to z. It is worth noting that z criteria are particularly difficult to meet, as any minor distortion in x gets amplified due to the derivative):

$$FFD(z, y') = |FF(z) - FF(y')| = \left| \frac{RMS(z)}{AVG(|z|)} - \frac{RMS(y')}{AVG(|y'|)} \right| \quad (48)$$

- The Pearson coefficient:

$$d_{pearson}(x, y) = \frac{\int [y(t) - AV\ (y)][x(t) - AVG(x)] dt}{\sqrt{\int [y(t) - AVG(y)]^2 dt \ \int [x(t) - AV\ (x)]^2 dt}} \quad (49)$$

- The Total Harmonic Distortion (applied only to z):

$$THD(z) = \frac{\sqrt{\sum_{k=2}^{+\infty} z_k^2}}{z} \quad (50)$$

Tab. 1 – Accuracy criteria of the methods described in this section.

Source	Euclidean Difference	Form Factor	Pearson Coefficient	Other
[24] P-ILC				Amplitude error < 0.2%
[41] QNM		1.11 ± 1%		Distortion < 1%
[43] LSM-PI		1.11 ± 0.1%		THD < 0.1%
[21] PhC-MGD		1.11 ± 0.1%	> 1 - 10^{-5}	Amplitude error < 0.1%
[44]	< 0.3% (magnitudes and phases)			
[40] PhC-P-ILC		1.11 ± 1%		THD < 1%; Amplitude error < 0.1%

- The Amplitude Error:

$$AE(x,y) = \frac{(x_{max}-x_{min})-(y_{max}-y_{min})}{x_{max}-x_{min}} \quad (51)$$

Table 1 provides the target values as applied in the literature. Even if different waveforms can have the same form factor [20][41], the IEEE standards recommend the use of this criterion for the magnetic hysteresis and losses characterization [49][50]. It is unsurprising to find it applied in many studies. For the MBN_{energy} characterization, we found it relevant to apply the following criteria:

- Relative Euclidean Difference < 0.5%
- z Form Factor = $F_{goal} \pm 0.5\%$
- Pearson coefficient > $1 - 3 \cdot 10^{-5}$
- z THD < 0.5%

III. Numerical Implementation

In our quest toward the "best" iterative method for MBN_{energy} hysteresis cycles, characterization, and STL application, all the techniques described in section 2 have been numerically implemented using MATLAB®. A sigmoid-type anhysteretic behavior (Eq. 52) has been used to simulate the material's answer:

$$y_M(t,j) = f[x(t,j)] = \frac{2}{\pi}\arctan[x(t,j)] \quad (52)$$

Eq. (52) is convenient as saturation is taken into account, and x_G can be expressed analytically:

$$x_G(t) = \tan\left(\frac{\pi}{2}y_G(t)\right) \quad (53)$$

The objective is to find x_G leading to a sinusoidal y_G. A preliminary test consists in plotting the spectral content of x_G as a function of y_G's amplitude (Fig. 3).

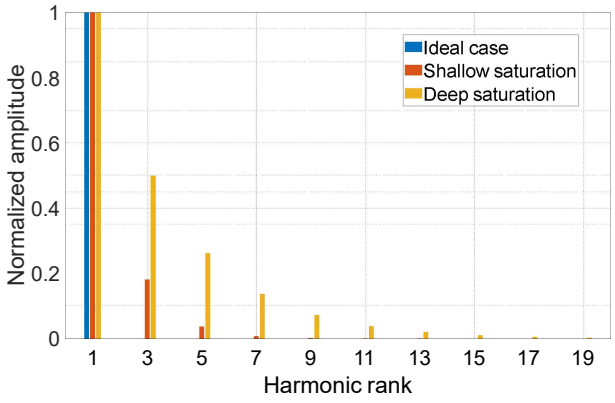

Fig. 3 – x_G harmonic content vs. y_G amplitude.

When y_G's amplitude is large, high amplitude harmonics are generated, triggering issues if the power source dynamic performance is limited. Waveform control is easier at low amplitude (no saturation and quasi-linear material behavior). THD of x_G can reach 0% at very low amplitudes, it however increases up to 18% at $0.75 \cdot \max(y_G)$ and even 51% at $0.95 \cdot \max(y_G)$. THD values exceeding 100% are possible if no control is applied [20], and this is expected to occur for even deeper saturation. No noise has been considered in all the following tests. The power amplifier is supposed to be ideal (infinite bandwidth, etc.), with perfect impedance matching. The sampling frequency has been reduced to 500 Hz to limit the memory allocation and reach convergence even with QNM.

A. Shallow saturation

The tested methods are firstly compared in a shallow saturation case:

$$y_G(t) = 0.75\sin(2\pi t) \quad (54)$$

The simulations are stopped when the Relative Euclidean Difference or the Form Factor Difference falls below 10^{-10}. The maximum iteration number is set to 600. On the one hand, such low error is only achievable in simulation; experimental conditions are affected by white noise, drifts, etc. On the other hand, such high accuracy allows testing the methods with y_M extremely close to y_G. Table 2 gives the simulation parameters, and Fig. 4 the simulation results.

Tab. 2 – Shallow saturation simulation parameters.

	Parameters
P-ILC, FDP-ILC	$k_P = 2.77$
FSP-ILC	$k_P = 2.77$, $N_{HARMONICS} = 200$
PhC-P-ILC	$K_P = 4.4$, $k_\alpha = 0$
PhC-MGD	$G_{PH} = 0$, $K_P = 1$
QNM	Same parameters as in [29], except $\lambda = 0.5$ and $\beta = 0.6$
LSM-PI	$N_{POWERS} = 45$

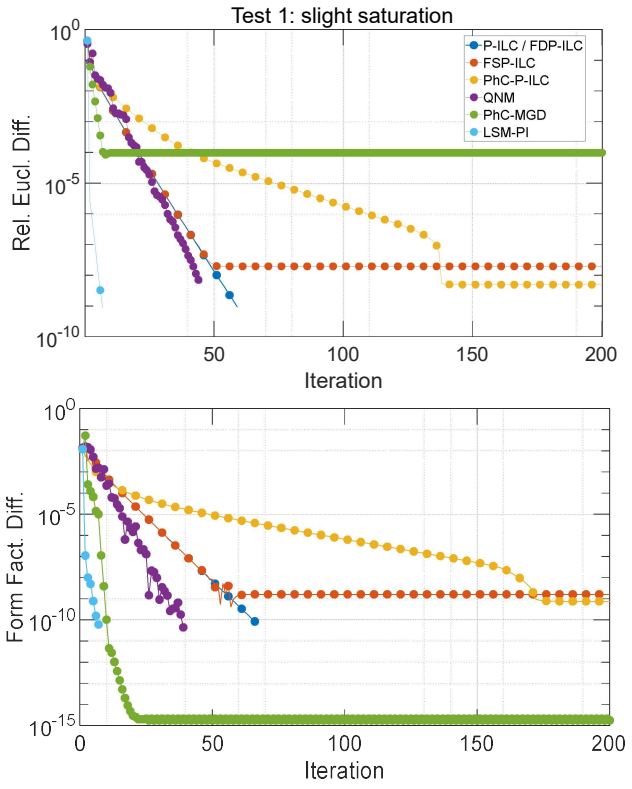

Fig. 4 – Relative Euclidean and form factor differences for the shallow saturation test.

Convergence is obtained for all the methods tested. LSM-PI and PhC-MGD are the fastest, with approximately 10 iterations. Still, for both these methods, the amplitude correction step requires a lot of intermediary measurements, which can be problematic in the low-frequency range. QNM converges after

40 iterations but needs long calculation times. P-ILC follows with around 60 iterations and minimal calculation times. Finally, FSP-ILC converges after almost 180 iterations. It is worth noting the residual error on P-ILC and FSP-ILC inherent to those methods and impossible to remove. Table 3 concludes this first set of tests by comparing the methods based on the criteria described in sub-section 2.1:

Tab. 3 – Performance comparison for the shallow saturation test.

	Num. of iter.	Num. of meas.	Fin. rel. euc. diff.	Final form factor	Calc. time per iter. (s)	Total calc. time (s)
P-ILC	66	66	$< 10^{-10}$	$8.9 \cdot 10^{-10}$	$4.7 \cdot 10^{-4}$	0.031
FDP-ILC	66	66	$< 10^{-10}$	$8.9 \cdot 10^{-10}$	$4.2 \cdot 10^{-4}$	0.023
FSP-ILC	60	60	$2.5 \cdot 10^{-8}$	$1.6 \cdot 10^{-9}$	0.008	0.47
PhC-P-ILC	174	174	$2.2 \cdot 10^{-9}$	$7.6 \cdot 10^{-10}$	0.01	1.7
PhC-MGD	11	196	$9.9 \cdot 10^{-5}$	$< 10^{-10}$	0.031	0.338
QNM	40	90	$1.4 \cdot 10^{-8}$	$< 10^{-10}$	0.52	20.92
LSM-PI	7	192	$9.0 \cdot 10^{-10}$	$< 10^{-10}$	0.39	2.743

Table 3 "calculation time" only considers the waveform identification computation time, i. e., it does not include additional times associated with virtual measurement simulation (equivalent to the measurement time in the experimental setup).

B. *Deep saturation*

In the next test, the iteration methods are tested closer to a fully saturated configuration, where larger non-linearity is present:

$$y_G(t) = 0.95 \sin(2\pi t) \tag{55}$$

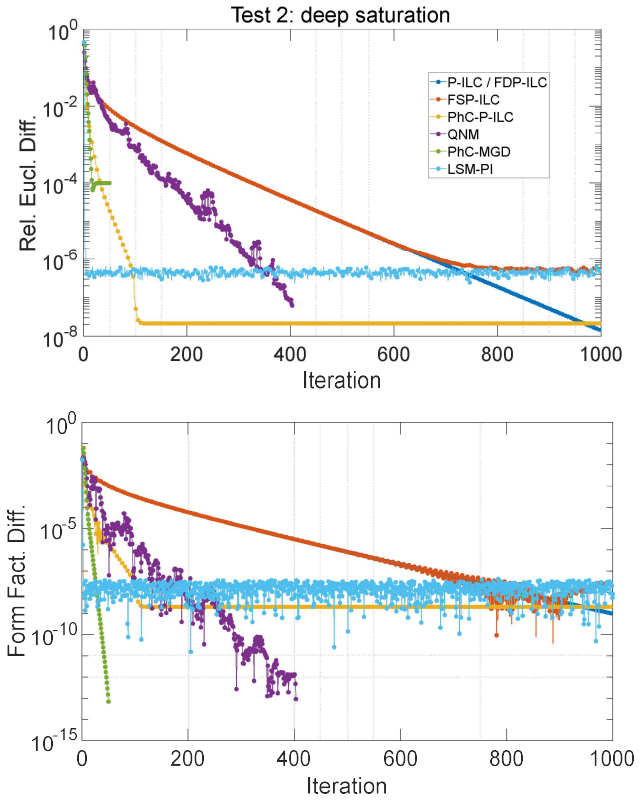

Fig. 5 – Relative Euclidean and form factor differences for the deep saturation test.

The maximum iteration number is raised to 1500 since overall convergence is slower in this case. Fig. 5 gives the simulation results, and Table. 4 the simulation parameters.

Tab. 4 – Deep saturation simulation parameters

	Parameters
P-ILC, FDP-ILC	$k_P = 3$
FSP-ILC	$k_P = 3$, $N_{HARMONICS} = 200$
PhC-P-ILC	$K_P = 5.6$, $k_\alpha = 0$
PhC-MGD	$G_{PH} = 0$, $K_P = 0.4$
QNM	Same parameters as in [29], except $\lambda = 0.5$ and $\beta = 0.5$
LSM-PI	$N_{POWERS} = 70$

Again, QNM and PhC-MGD show the fastest convergence speed. PhC-P-ILC is also very fast, outclassing QNM, exhibiting temporary convergence errors. P-ILC converges slowly for this test, but unlike PhC-P-ILC, it never gets stuck on a precision plateau. Table 5 compares the performances. The precision criterion is set to $< 10^{-7}$.

Tab. 5 – Performance comparison for the deep saturation test.

	Num. of iter.	Num. of meas.	Fin. rel. euc. diff.	Final form factor	Calc. time per iter. (s)	Total calc. time (s)
P-ILC	653	653	$1.29 \cdot 10^{-6}$	$< 10^{-7}$	$2.7 \cdot 10^{-4}$	0.176
FDP-ILC	653	653	$1.29 \cdot 10^{-6}$	$< 10^{-7}$	$4.2 \cdot 10^{-4}$	0.272
FSP-ILC	637	637	$1.69 \cdot 10^{-6}$	$< 10^{-7}$	0.009	5.97
PhC-P-ILC	87	87	$9.97 \cdot 10^{-7}$	$< 10^{-7}$	0.012	1.02
PhC-MGD	24	3182	$9.78 \cdot 10^{-5}$	$< 10^{-7}$	0.19	4.61
QNM	179	484	$9.57 \cdot 10^{-5}$	$< 10^{-7}$	0.49	88.8
LSM-PI	3	3161	$2.03 \cdot 10^{-6}$	$< 10^{-7}$	2.21	6.63

A high number of iterations limits LSM-PI and PhC-MGD performances. QNM's iterations number is lower, but each requires a significant calculation time. The PhC-P-ILC method converges with a reduced number of iterations, eight times lower than P-ILC, but the calculation time for the latter is extremely short.

C. *Overall simulation results*

Table 6 compiles the comparisons based on the performance criteria defined in sub-section 2.1.

Tab. 6 – Performances comparison based on the performance criteria defined in sub-section 2.1.

	Num. of var.	Exec. time (per iter.)	Conv. speed	Preci sion	Achiev. samp. Freq.	Robu stness
P-ILC / FDP-ILC	**1**	**Low**	Low-Med.	**High**	**High**	**High**
FSP-ILC	**1**	Med.	Low-Med.	Med.	**High**	**High**
PhC-P-ILC	2	Med.	Med.	**High**	**High**	**High**
PhC-MGD	2	Med.	**High**	**High**	Med.	Low
QNM	6	High	**High**	**High**	Low	Low
LSM-PI	N	Very high	**High**	**High**	Med.	Low

MBN_{energy} measurements require high sampling frequency, up to several hundreds of kHz, and long-time measurements leading to huge memory size for numerical feedback variables.

Methods that rely on matrix inversions like QNM or parameter optimization like LSM-PI are unsuitable. This issue can be partially solved by downsampling the signals, applying correction, and upsampling the resulting waveforms by interpolation (PhC-MGD [21]). But it means complexity and uncertainty in the measurement treatment. White noise's consequence on the working signals is another issue to consider. Methods like PhC-MGD require an intense averaging process to reach convergence which means extended time acquisition (several cycles) or a sliding window filter. These treatments bring complexity in the signals processing and potentially additional phase delays. Since B_a is obtained by integrating a noisy signal, a drift is always expected. Such a drift can be problematic on methods that normalize signals or expect y_M to have a specific amplitude (PhC-MGD, LSM-PI). A pre-treatment on B_a is required to reach convergence. Oppositely, P-ILC does not require a perfect drift compensation to reach convergence. After all the numerical tests performed in this study, and based on Table 6 analysis, P-ILC appears to be the most adapted method in the context of the $MBN_{energy}(H_{surf})$ hysteresis cycles characterization. In the next section, improvements are proposed for even better and faster convergence.

IV. P-ILC EXTENSIONS

P-ILC is an excellent method for magnetization control digital feedback. P-ILC is simple to implement and tune. It is robust and fast. Its only limitation comes from the convergence speed, especially near saturation when the permeability falls and where a weak variation of H_{surf} generates an even lower variation of B_a. This problem can be partially solved by increasing the proportional gain, but the response will diverge in the high permeability zones. A better solution consists in modulating K_p according to the system answer:

$$x(t, j+1) = x(t, j) + K_P(t, j)\epsilon(t, j) \quad (56)$$

This method requires additional parameters and should be considered with special attention. It can be implemented from an error array based on the two previous iterations (P-ILC-2 [51]) and give Eq. 57:

$$x(t, j+2) = x(t, j+1) + K_{P_1}\epsilon(t, j+1) + K_{P_2}\epsilon(t, j) \quad (57)$$

The resulting error becomes a weighted sum of j+1 and j errors iterations. A generalized version (P-ILC-N) considering all the previous state N can even be written by extending Eq. 57:

$$x(t, j+N) = x(t, j+N-1) + \sum_{q=1}^{N} K_{P_q}\epsilon(t, j+N-q) \quad (58)$$

P-ILC-N convergence is faster. It is also more robust than standard P-ILC [51]. But a minimum of N measurements are necessary for the corrector to be fully working. All K_{P_q} coefficients need to be optimized individually, which can be complex and demanding in experimental data. Hence, N should be kept as small as possible unless a reliable model is available for simulation. Another possibility consists of structuring the P-ILC iterative law as a Taylor approximation (assuming x is a y_M smooth function):

$$x(y_G) = x(y_M) + A(y_M)(y_G - y_M) \quad (59)$$

If $x(t,j+1) = x_G(t)$, higher orders Taylor approximation gives P-ILC-TA, Eq. 60:

$$x(t, j+1) = x(t, j) + \sum_{s=1}^{N} K_{P_s}\epsilon(t, j)^s \quad (60)$$

It is also possible to replace A in Eq. 59 with its optimal value, as obtained by the Taylor's approximation (P-ILC-TD):

$$x(y_G) = x(y_M) + \frac{dx}{dy}(y_M)(y_G - y_M) \Rightarrow \frac{dx}{dy} = \frac{1}{\frac{dy}{dx}} \propto \frac{1}{\mu} \quad (61)$$

$$\Rightarrow K_P(t, j) = \frac{dx}{dy_M}(t, j) \quad (62)$$

P-ILC-TD can reach high-speed convergence rates. K_p being inversely proportional to the system reactivity, the correction will be significant when dy_M/dx is small. However, relying on derivatives, P-ILC-TD requires exact measurement, no noise, delays, or bandwidth limitations. Otherwise, this method diverges very quickly. Finally, the deep saturation test (sub-section 3.2) was repeated, and all P-ILC new variants were tested. Fig. 6 shows the simulation results, and Table 7 shows the corresponding iteration numbers.

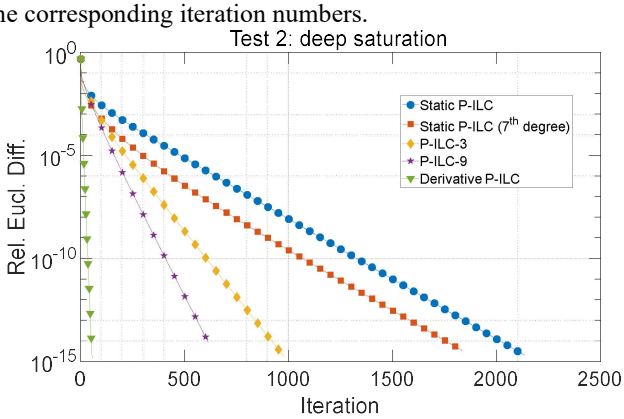

Fig. 6 – Relative Euclidean differences, deep saturation test for the different P-ILC methods.

Tab. 7 – Comparative results based on the iterations number before convergence.

	Number of iterations
P-ILC	2135
P-ILC-TA (7th degree)	1835
P-ILC-3	979
P-ILC-9	613
P-ILC-TD	55

All alternative methods converge faster than P-ILC. P-ILC-TD outclasses all the proposed methods. An iterative process close to P-ILC-TD robust enough to handle white noise would be by far the most indicated method.

V. EXPERIMENTAL SETUP AND IMPLEMENTATION

The experimental setup used for the Barkhausen noise characterization has been precisely described in [19]. The excitation of the sample is based on single C-yoke with the magnetizing winding, and with the sensors attached to the sample under test. An overall 2D view of this experimental setup is depicted in Fig. 7.

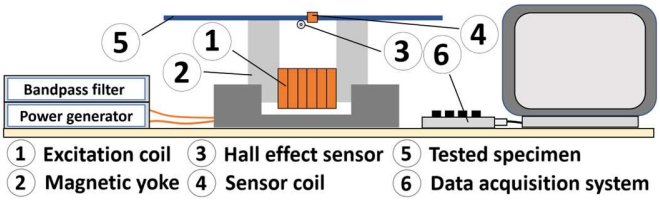

Fig. 7 – Overall 2D view of the Barkhausen noise experimental setup.

The power amplifier was a Kepco BOP100-10MG. The excitation coil was made out of 10 turns. The studied specimens were all grain-oriented electrical steels (FeSi GO 3wt%, M140-27). Their dimensions were 280 x 30 x 0.3 mm, with the length in the easy magnetization direction. Two 120 turns coils were wound around the specimen and plugged in opposite directions as recommended in [52]. The distance separating the sensor coils was set arbitrarily to 10 mm, as used in the previous work [19][53][54] by the authors. The influence of this distance has not been investigated in detail. Two Krohn-Hite 3362 amplifiers-filters were used for the signal conditioning and a National Instruments DAQ USB-6346 acquisition card, controlled through a GUI in Python and of 500 kHz sampling frequency for their acquisitions. Python® and Matlab® were used for the numerical treatment. Eq. (63) - (65) summarized all the tests carried out:

$$B_a(\text{goal}) = B\sin(2\pi f_{exc}t) \quad (63)$$

$$B = 1.8\ \text{T} \quad (64)$$

$$f_{exc} = \{0.2,\ 2,\ 20,\ 200\}\ \text{Hz} \quad (65)$$

P-ILC was used to set the current waveforms. Fig. 8 depicts the experimental results obtained on three decades of frequency and B_a equal to 1.8 T, i.e., the worst-case analyzed scenario in terms of non-linear behavior.

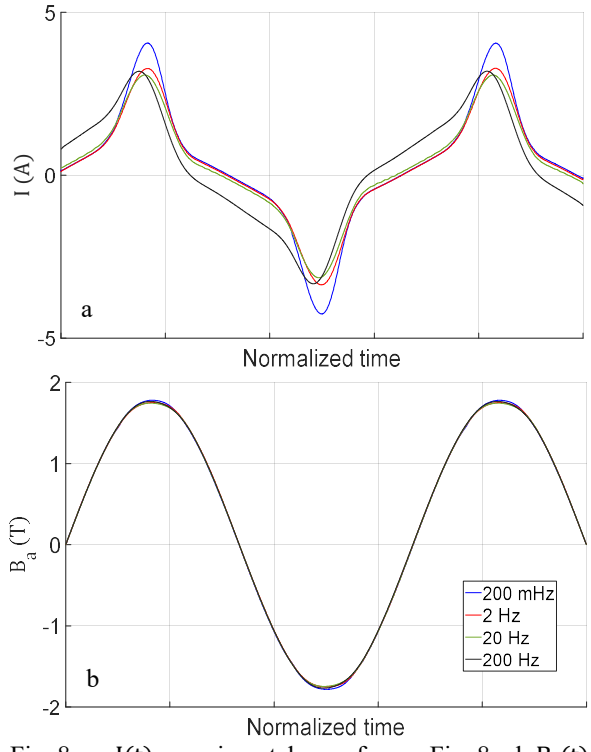

Fig. 8 – a I(t) experimental waveforms, Fig. 8 – b B_a(t) experimental waveforms,

The 200 mHz current peak is unexpectedly high as compared to other frequencies. However, this difference could be caused simply by the non-linearity of the magnetic material because of the larger difference in amplitude as evident from Table 8. Table 8 summarizes the accuracy of the experimental results by comparing them using sub-section 2.3 criteria.

Tab. 8 – Experimental performances comparison based on the accuracy criteria defined in sub-section 2.3.

	200 mHz	2 Hz	20 Hz	200 Hz	Goal (Int. stand.)
Euc. Dist. (%)	0.678	0.35	0.57	0.34	< 0.5
Pears. Coef.	0.9999897	0.99999394	0.9999841	0.99999438	> 0.99997
Form Fact. Diff. (dB/dt)(%)	0.74	0.29	0.14	0.31	< 0.5
Amp. Diff. (%)	0.96	0.27	0.05	0.3	< 1
THD (dB/dt) (%)	5.33	1.4	2.95	3.7	< 0.5

Criteria met Criteria not met

Some Fig. 8 experimental results do not reach the accuracy targeted by the international standards. On the first hand, these standards imposed tight specifications of the experimental conditions (geometry, measurements, etc.), far from the experimental setup depicted in Fig. 7. IEC 60404-3 [50] related to the single sheet tester imposed by instant to use a top and a bottom yoke of large dimensions as displayed in Fig. 9.

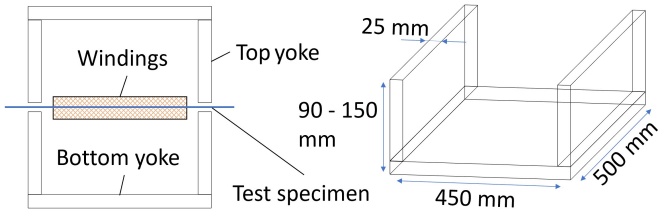

Fig. 9 – IEC 60404-3 single sheet tester illustration and yoke dimensions

On the other hand, Fig. 7 setup has been designed based on usual MBN observation methods, like in a non-destructive testing context where magnetization waveform control is not required and never done (see [55]-[58] for examples). This setup delivers magnetic excitation significantly less homogeneous compared to those of [50], and the volume of the tested specimen is reduced. These limitations result in a considerable increase in the magnetization control complexity, justifying a lower accuracy in Table 8 results.

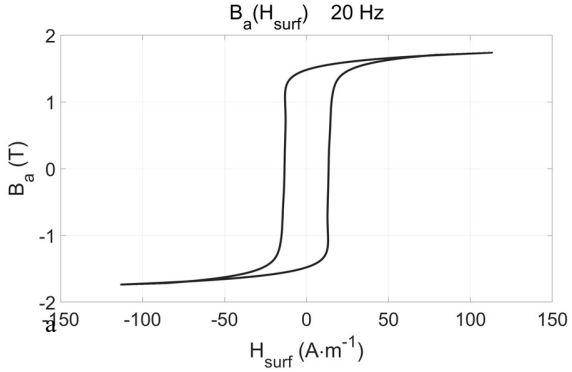

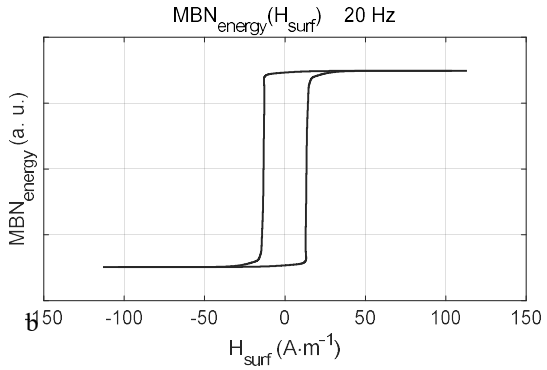

Fig. 10 – a $B_a(H_{surf})$ experimental hysteresis cycle, Fig. 10 – b $MBN_{energy}(H_{surf})$ renormalized experimental hysteresis cycles.

A phase delay was also noticed between I(t) and $B_a(t)$. This delay could be a source of divergence for some ILC algorithms (like QNM, whose core assumption relies on the $I(B_a)$ bijectivity). Finally, Fig. 10 shows, as examples, the 20 Hz, 1.8 T sinus flux density, $B_a(H_{surf})$, and $MBN_{energy}(H_{surf})$ measured cycles. Differences can be observed between the experimental $MBN_{energy}(H_{surf})$ and the $B_a(H_{surf})$ hysteresis cycles. Those differences were expected and can be explained as follows:

- All magnetization contributions are involved in the $B_a(H_{surf})$ hysteresis cycles, mainly the domain wall motions and the magnetization rotation.
- For the $MBN_{energy}(H_{surf})$ cycle, the contribution is limited to the domain wall motions.

It is worth noting the difference at saturation once the cycle is closed. On the first hand, the $MBN_{energy}(H_{surf})$ cycle reaches a flat saturation. No more variation of the MBN_{energy} is observed, reflecting the entire disappearance of the domain wall motions. On the other hand, the $B_a(H_{surf})$ still varies. The magnetization rotation remains active and increases the magnetic flux density. The differences are expected to be even more pronounced in the higher frequency range. When $B_a(H_{surf})$ cycles reflect all STL contributions, the $MBN_{energy}(H_{surf})$ ones are limited to the domain wall motion contributions excluding, notably, the classical loss contribution.

VI. Conclusion

Studying the magnetization mechanisms in magnetic cores is a genuine problem that has generated substantial research efforts. A fine study of the $MBN_{energy}(H_{surf})$ hysteresis cycle excitation frequency dependency and its prediction through an STL-like theory is expected to bring insights into the physical behavior of the magnetization mechanisms.

For this, the flux density has to be imposed sinusoidal from the quasi-static state up to approximately a few hundred Hz, depending on the nature of the tested specimen. Such control might be seen as a simple problem. Still, because of the strong linearities, the practical aspect happens to be especially complex, hence the proliferation of the feedback algorithms in the literature ([40]-[43] are good examples).

In this study, the theoretical problem of B_a control on a classic setup (yoke and sample) has been established, and the ILC (the iterative version of the classic PID controller) has been explained. Different ILC settings exist, and a detailed review of these methods was done in the second section of this manuscript providing valuable insights generalizable to every waveform control environment. For a proper choice, the experimental conditions and the final objective have to be perfectly defined from the very beginning.

Then, six performance criteria have been proposed to identify the most adapted method in the specific context of the $MBN_{energy}(H_{surf})$ hysteresis cycle characterization, and numerical tests were performed for a comparison purpose followed by conclusions.

P-ILC gave the best performance and the highest satisfaction rate. It was therefore chosen for experimental implementation. Experimental tests were realized on a wide range of amplitude and frequency. We noticed, as expected, a more significant error for higher frequency (limitations of the practical setup bandwidth) and amplitude (stronger non-linear behavior of the tested specimen).

References

[1] Fiorillo, F. (2005). *Measurement and characterization of magnetic materials (electromagnetism)*. Elsevier Academic Press.
[2] Steinmetz, C. P. (1892). On the law of hysteresis. *Transactions of the American Institute of Electrical Engineers*, *9*(1), 1-64.
[3] Reinert, J., Brockmeyer, A., & De Doncker, R. W. (2001). Calculation of losses in ferro-and ferrimagnetic materials based on the modified Steinmetz equation. *IEEE Transactions on Industry applications*, *37*(4), 1055-1061.
[4] Jordan, H. (1924). Die ferromagnetischen Konstanten für schwache Wechselfelder. *Elektr. Nach. Techn*, *1*(8).
[5] Krings, A., & Soulard, J. (2010). Overview and comparison of iron loss models for electrical machines. *Journal of Electrical Engineering*, *10*(3), 8-8.
[6] Krall, F. (2017). Analysis and implementation of algorithms for calculation of iron losses for fractional horsepower electric motors.
[7] Goss, N. P. (1934), U.S. Patent 1965 559.
[8] Shilling, J., & Houze, G. (1974). Magnetic properties and domain structure in grain-oriented 3% Si-Fe. *IEEE Transactions on Magnetics*, *10*(2), 195-223.
[9] Bertotti, G. (1998). *Hysteresis in magnetism: for physicists, materials scientists, and engineers*. Gulf Professional Publishing.
[10] Bertotti, G., Fiorillo, F., & Soardo, G. P. (1988). The prediction of power losses in soft magnetic materials. *Le Journal de Physique Colloques*, *49*(C8), C8-1915.
[11] Atallah, K., & Howe, D. (1994). The calculation of iron losses in brushless permanent magnet dc motors. *Journal of magnetism and magnetic materials*, *133*(1-3), 578-582.
[12] Amar, M., & Kaczmarek, R. (1995). A general formula for prediction of iron losses under nonsinusoidal voltage waveform. *IEEE Transactions on Magnetics*, *31*(5), 2504-2509.
[13] Leicht, J. (2003), Magnetic properties of electrical steel under controlled magnetisation conditions, PhD Thesis, University of Wales, Cardiff, UK.
[14] Leicht, J., Moses, A. J., & Zurek, S. (2008). Hysteresis loss component under non-sinusoidal flux waveforms. *Journal of Magnetism and Magnetic Materials*, *320*(20), e608-e610.
[15] Ragusa, C., Zhao, H., Appino, C., Khan, M., de la Barrière, O., & Fiorillo, F. (2016). Loss decomposition in non-oriented steel sheets: the role of the classical losses. *IEEE Magnetics Letters*, *7*, 1-5.
[16] Zhao, Z., & Hu, X. (2020). Modified loss separation in FeSi laminations under arbitrary distorted flux. *AIP Advances*, *10*(8), 085222.
[17] Ducharne, B., Le, M. Q., Sebald, G., Cottinet, P. J., Guyomar, D., & Hebrard, Y. (2017). Characterization and modeling of magnetic domain wall dynamics using reconstituted hysteresis loops from Barkhausen noise. *Journal of Magnetism and Magnetic Materials*, *432*, 231-238.
[18] Ducharne, B., Gupta, B., Hebrard, Y., & Coudert, J. (2018, April). Characterization and local phenomenological model of Barkhausen noise under mechanical and magnetic excitations. In *2018 IEEE International Magnetics Conference (INTERMAG)* (pp. 1-1). IEEE.
[19] Fagan, P., Ducharne, B., Daniel, L., & Skarlatos, A. (2021). Multiscale modelling of the magnetic Barkhausen noise energy cycles. *Journal of Magnetism and Magnetic Materials*, *517*, 167395.

[20] Zurek, S. (2017). *Characterisation of soft magnetic materials under rotational magnetisation*. CRC Press.
[21] Stupakov, A., Perevertov, O., & Zablotskii, V. (2015). A system for controllable magnetic measurements of hysteresis and Barkhausen noise. *IEEE Transactions on Instrumentation and Measurement*, *65*(5), 1087-1097.
[22] Stupakov, A., & Perevertov, A. (2020). Analog of the induction law for the magnetic Barkhausen noise. *Journal of Magnetism and Magnetic Materials*, *498*, 166238.
[23] Grote, N., Denke, P., Rademacher, M., Kipscholl, R., Bongards, M., & Siebert, S. (1998). Measurement of the magnetic properties of soft magnetic material using digital real-time current control. *Nonlinear Electromagnetic Systems*, 566-569.
[24] Zurek, S. (2017). Practical implementation of universal digital feedback for characterisation of soft magnetic materials under controlled AC waveforms. *Przeglad Elektrotechniczny*, *93*(7), 16-21.
[25] Bertotti, G., Ferrara, E., Fiorillo, F., & Pasquale, M. (1993). Loss measurements on amorphous alloys under sinusoidal and distorted induction waveform using a digital feedback technique. *Journal of applied physics*, *73*(10), 5375-5377.
[26] Birkelbach, G., Hempel, K., & Schulte, F. (1986). Very low frequency magnetic hysteresis measurements with well-defined time dependence of the flux density. *IEEE Transactions on Magnetics*, *22*(5), 505-507.
[27] Matsubara, K., Takahashi, N., Fujiwara, K., Nakata, T., Nakano, M., & Aoki, H. (1995). Acceleration technique of waveform control for single sheet tester. *IEEE transactions on magnetics*, *31*(6), 3400-3402.
[28] Zemánek, I. (2003). Exciting signal generator for SSTs. *Journal of magnetism and magnetic materials*, *254*, 73-75.
[29] Zhang, Y., Long, Y., Qu, Q., Ye, R., & Chang, Y. (2007). Precise AC magnetic measurement under sinusoidal magnetic flux by using digital feedback of harmonic compensation. *Journal of magnetism and magnetic materials*, *312*(2), 443-448.
[30] White, S., Krause, T. W., & Clapham, L. (2012). A multichannel magnetic flux controller for periodic magnetizing conditions. *IEEE Transactions on Instrumentation and Measurement*, *61*(7), 1896-1907.
[31] Baranowski, S., Tumanski, S., & Zurek, S. (2009). Comparison of digital methods of the control of flux density shape. *Przegląd Elektrotechniczny*, *85*, 93-95.
[32] Hollitscher, H. (1969). Core losses in magnetic materials at very high flux densities when the flux is not sinusoidal. *IEEE Transactions on Magnetics*, *5*(3), 642-647.
[33] Pólik, Z., & Kuczmann, M. (2008). Measuring and control the hysteresis loop by using analog and digital integrators. *J. Optoelectron. Adv. Mater*, *10*(7), 1861-1865.
[34] Song, Y., Gong, Y., & Kuo, S. M. (2005). A robust hybrid feedback active noise cancellation headset. *IEEE transactions on speech and audio processing*, *13*(4), 607-617.
[35] Ludke, J., & Ahlers, H. (2001). Hybrid control used to obtain sinusoidal curve form for the power loss measurement on magnetic materials. In *Materials Science Forum* (Vol. 373, pp. 469-472). Trans Tech Publications Ltd., Zurich-Uetikon, Switzerland.
[36] Patel, H. V., Zurek, S., Meydan, T., Jiles, D. C., & Li, L. (2006). A new adaptive automated feedback system for Barkhausen signal measurement. *Sensors and Actuators A: Physical*, *129*(1-2), 112-117.
[37] Gruebler, H., Krall, F., Leitner, S., & Muetze, A. (2018, September). Loss-surface-based iron loss prediction for fractional horsepower electric motor design. In *2018 20th European Conference on Power Electronics and Applications (EPE'18 ECCE Europe)* (pp. P-1). IEEE.
[38] Freeman, C. T., Lewin, P. L., & Rogers, E. (2005). Experimental evaluation of iterative learning control algorithms for non-minimum phase plants. *International Journal of Control*, *78*(11), 826-846.
[39] Freeman, C. T., Tong, D., Meadmore, K., Cai, Z., Rogers, E., Hughes, A. M., & Burridge, J. H. (2011). Phase-lead iterative learning control algorithms for functional electrical stimulation-based stroke rehabilitation. *Proceedings of the Institution of Mechanical Engineers, Part I: Journal of Systems and Control Engineering*, *225*(6), 850-859.
[40] Zurek, S., Marketos, P., Meydan, T., & Moses, A. J. (2005). Use of novel adaptive digital feedback for magnetic measurements under controlled magnetizing conditions. *IEEE Transactions on Magnetics*, *41*(11), 4242-4249.
[41] Yamamoto, K. I., & Hanba, S. (2008). Waveform control for magnetic testers using a quasi-Newton method. *Journal of Magnetism and Magnetic Materials*, *320*(20), e539-e541.
[42] Li, D. H., & Fukushima, M. (2000). A derivative-free line search and global convergence of Broyden-like method for non-linear equations. *Optimization methods and software*, *13*(3), 181-201.
[43] Anderson, P. (2011). Constant dB/dt DC characterisation through digital control of magnetic field. *Przeglad Elektrotechniczny*, *87*(9b), 77-78.
[44] Zhang, C., Li, Y., Li, J., Yang, Q., & Zhu, J. (2016). Measurement of three-dimensional magnetic properties with feedback control and harmonic compensation. *IEEE Transactions on Industrial Electronics*, *64*(3), 2476-2485.
[45] White, S., Krause, T., & Clapham, L. (2007). Control of flux in magnetic circuits for Barkhausen noise measurements. *Measurement Science and Technology*, *18*(11), 3501.
[46] Bosack, M., Kollmer, J., Niemoczynski, B., & Biswas, S. (2014, August). Closed loop control of hysteretic magnetization. In *2014 7th International Symposium on Resilient Control Systems (ISRCS)* (pp. 1-6).
[47] Havlicsek, H., & Alleyne, A. (1999). Non-linear control of an electrohydraulic injection molding machine via iterative adaptive learning. *IEEE/ASME transactions on mechatronics*, *4*(3), 312-323.
[48] Heertjes, M., & Tso, T. (2007). Non-linear iterative learning control with applications to lithographic machinery. *Control Engineering Practice*, *15*(12), 1545-1555.
[49] IEC 60404-2, "Magnetic materials – Part 2: Methods of measurement of the magnetic properties of electrical steel strip and sheet by means of an Epstein frame," *International Electrotechnical Commission*, June 2008.
[50] IEC 60404-3, "Magnetic materials – Part 3: Methods of measurement of the magnetic properties of electrical steel strip and sheet by means of a single sheet tester," *International Electrotechnical Commission*, April 2010.
[51] Zheng, Y., Liu, X., Zhao, J., Mo, N., & Shi, Z. (2020). A novel iterative learning control method and control system design for active magnetic bearing rotor imbalance of primary helium circulator in high-temperature gas-cooled reactor. *Measurement and Control*, *53*(3-4), 474-484.
[52] Moses, A. J., Patel, H. V., & Williams, P. I. (2006). AC Barkhausen noise in electrical steels: Influence of sensing technique on interpretation of measurements. *Journal of Electrical Engineering*, *57*(8), 3-8.
[53] Fagan, P., Ducharne, B., Daniel, L. and Skarlatos, A., 2021. Magnetic Barkhausen noise: A simulation tool. *AIP Advances*, *11*(2), p.025322.
[54] Fagan, P., Ducharne, B., Daniel, L., Skarlatos, A., Domenjoud, M. and Reboud, C., 2022. Effect of stress on the magnetic Barkhausen noise energy cycles: A route for stress evaluation in ferromagnetic materials. *Materials Science and Engineering: B*, *278*, p.115650.
[55] Stewart, D. M., Stevens, K. J., & Kaiser, A. B. (2004). Magnetic Barkhausen noise analysis of stress in steel. *Current Applied Physics*, *4*(2-4), 308-311.
[56] Perez-Benitez, J. A., Capo-Sanchez, J., Anglada-Rivera, J., & Padovese, L. R. (2008). A study of plastic deformation around a defect using the magnetic Barkhausen noise in ASTM 36 steel. *Ndt & e International*, *41*(1), 53-58.
[57] Soto, M., Martinez-de-Guerenu, A., Gurruchaga, K., & Arizti, F. (2009). A completely configurable digital system for simultaneous measurements of hysteresis loops and Barkhausen noise. *IEEE Transactions on instrumentation and measurement*, *58*(5), 1746-1755.
[58] Ding, S., Tian, G., Dobmann, G., & Wang, P. (2017). Analysis of domain wall dynamics based on skewness of magnetic Barkhausen noise for applied stress determination. *Journal of Magnetism and Magnetic Materials*, *421*, 225-229.